Available online at www.sciencedirect.com

ScienceDirect

Materials Today: Proceedings 5 (2018) 10097–10103

materialstoday: PROCEEDINGS

www.materialstoday.com/proceedings

IC-FNM 2016

Structural and optical properties of Sb doped SnO_2 nanopowders synthesized by nebulized spray pyrolysis

M. John Silvister Raju, S.S. Bhattacharya *

Nano Functional Materials Technology Center, Department of Metallurgical & Materials Engineering
Indian Institute of Technology Madras, Chennai, India 600 036

Abstract

Nebulized spray pyrolysis (NSP) was used to synthesize $Sn_{1-x}O_2$: Sb_x (x=0, 0.03, 0.06, 0.09) nanopowders in reasonable quantities by making use of low-cost precursors. Structural analysis was carried out by XRD, TEM, SEM and XPS. X-ray diffraction analysis confirmed the formation of phase-pure SnO_2 with Sb being incorporated into the crystal structure. Rietveld refinement was used to estimate the lattice parameters and by adopting spherical harmonics, the crystallite sizes were calculated. Transmission electron microscopy revealed that the as-synthesized powders had good crystallinity with particle sizes in the range of 5-15 nm, which was in accordance with crystallite sizes calculated from Rietveld refinement.XPS confirmed the presence of antimony in the doped samples. Optical transparency was evaluated by absorption spectroscopy, which revealed both pure and doped SnO_2 to have more than 80% transparency in the visible regime. The band gap energies were estimated from standard Tauc plots.

Selection and/or Peer-review under responsibility of International Conference on Functional Nano-Materials, 2016.

*Keywords:*Tin oxide, Nano powders synthesis; Spray Pyrolysis; Rietveld refinement; X-ray photoelectron spectroscopy;

1. Introduction

Nanocrystalline transparent conducting oxide (TCO) powders, such as ZnO, ITO and SnO_2, have been finding applications in optoelectronic devices, multifunctional windows, solar cells, flexible electronics and, more recently, transistors[1,2]. Tin Oxide (SnO_2) is a well-known n-type, wide band-gap semiconductor with transparency ~ 90%. SnO_2 possesses a tetragonal rutile structure with a space group of $P4_2/mnm$. Figure 1 gives the unit cell of SnO_2

* Corresponding author.Tel.: +91-44-2257 4765 ; fax: +91-44-2257 0509 .
*E-mail address:*ssb@iitm.ac.in

Selection and/or Peer-review under responsibility of International Conference on Functional Nano-Materials, 2016.

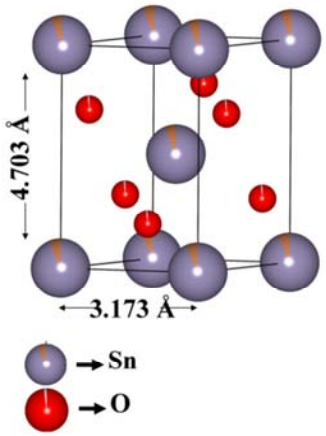

Figure 1 SnO_2 crystal structure

containing six atoms comprising of four oxygen atoms and two tin atoms. Each tin atom is surrounded by six oxygen atoms and each oxygen atom is surrounded by three tin atoms [3]. Standard lattice parameters of SnO_2 are a=b=4.307Å and c=3.173Å. In stochiometric bulk form, SnO_2 is an insulator [4], but the presence of oxygen deficiencies makes SnO_2 a semiconductor with a wide bandgap energy of 3.6 eV [5]. Substitutional doping with dopants increases the number of electrons in the conduction band and the plasma excitation wavelength shifts to shorter wavelengths which create a fundamental trade-off between transparency and conductivity[2,6]. The most common dopants in SnO_2 are Sb and F. Antimony doped tin oxide (ATO) can be an economical alternative to commercially available ITO not just because it is inexpensive but also for its comparable functional properties such as optical transparency, electrical conductivity, thermal and environmental stability [7]. Doped SnO_2 nanoparticles have been synthesized by various routes, such as co-precipitation [8,9], hydrothermal [10] and sol-gel [11,12]. However, most of these methods result in a high degree of agglomeration in the particles and mass production by these routes is difficult [13]. On the other hand, gas phase processing methods such as flame spray pyrolysis and chemical vapour synthesis can produce these nanopowders in bulk quantities with a high degree of crystallinity and purity [14–16].

The objective of the present investigation was to synthesize high purity, nanocrystalline antimony-doped tin oxide (ATO) nanopowders by a nebulized spray pyrolysis route, using easily available and inexpensive inorganic precursors.

2. Experimental

2.1. Nebulized spray pyrolysis (NSP)

The schematic of the NSP system used is shown in Figure 2. The main components of NSP were the gas and precursor flow system including the nebulizer, the hot wall reactor, the powder collector unit and the pumping system. The nebulizer atomizes the precursor solution into fine droplets by the assistance of compressed air. These droplets were carried into the hot wall reactor (tubular furnace) with/without an additional carrier gas. The supply of the gases was regulated by mass flow controllers, MFCs (MKS® systems). The furnace was set to a fixed temperature where pyrolysis of the precursor took place and nanopowders produced from the coalescence/coagulation of the generated monomers. The synthesized nanopowders were collected on a suitable filter in the powder collection unit and the vacuum in the system was maintained by the help of the pumping system. The system pressure was regulated with the help of a butterfly valve and an absolute pressure gauge (Baratron).

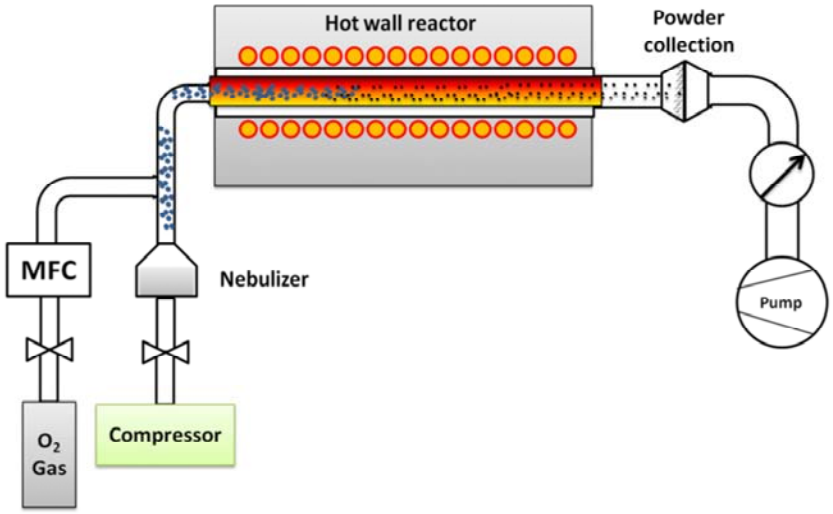

Figure 2 Schematic of Nebulized Spray Pyrolysis (NSP)

2.2. Synthesis

$SnCl_2.2H_2O$ (Alfa Aesar) was used as the tin source and, for the doped samples, $SbCl_3$ (Alfa Aesar) was used as the antimony source to prepare the precursor. The precursor solution was prepared in several steps. Tin chloride was first dissolved in ethanol with 1M concentration and in parallel, a 1M ethanol solution of antimony chloride was prepared. Once a clear solution of tin chloride with no precipitates was achieved after stirring for about 15 minutes, the antimony chloride solution was then added slowly dropwise. Stirring was continued to ensure that a clear solution was formed. For the current synthesis, a nebulizer of 10 mL capacity was taken, which can atomize the solution at the rate of 0.5 mL/min and no carrier gas was used. The temperature of the hot wall reactor was set at 1000°C. The powder was collected on filter papers and characterized in the as-synthesized form.

2.3. Characterization

X-ray diffraction (XRD) patterns were recorded using Cu Kα radiation at room temperature in a PANalytical® (X'pert Pro) diffractometer. A Bragg-Brentano geometry was used for measurements with 2 theta range from 20° to 80°, with a step size of 0.02°. A standard Si sample was used to determine and correct for the instrumental broadening. In order to get an accurate estimate of the structural parameters, Rietveld refinement was carried out using the FULLPROF® software. For this purpose, a slow scan was performed with a step size of 0.008° and scan time of 10s. Transmission electron micrographs were taken in an FEI-Tecnai™ G2 20F transmission electron microscope (TEM). The TEM samples were prepared by ultrasonically dispersing the powders in ethanol, following which few droplets were placed on carbon-coated Cu grids and dried for few hours. The X-ray photoelectron spectroscopy (XPS) studies were carried out on a SPECS X-ray photoelectron spectrometer system equipped with Mg radiation (Mg Kα, 1253.6 eV) as a probe and a PHOBIOS 100 MCD as an analyzer. During the XPS measurements, a chamber pressure of 5.9×10^{-9} Torr was maintained. Absorption spectroscopy was carried out for as-synthesized powders in an absorption spectrometer in the wavelength range from 100 nm to 1000 nm. The band-gap energies were computed by determining the absorption edge from the corresponding Tauc plots.

3. Results and discussion

3.1. Structural properties analysis by Rietveld refinement

For selected samples, Rietveld refinement was performed on the diffraction data to evaluate structural properties such as lattice parameters, occupancy etc,. Before carrying out refinement, the instrumental broadening was eliminated using Le Bail fit of the standard silicon XRD data. Standard structural parameters of the cassiterite polymorph of SnO_2 having a tetragonal crystal structure with the space group of $P4_2/mnm$ were taken as input. Sn^{4+} atoms were considered to be at 2(a) Wyckoff position, (0,0,0;1/2,1/2,1/2) and O^{2-} atoms at 4(f) Wyckoff position, ±(x,x,0;1/2+x,1/2-x,1/2) and with x=0.306. For antimony doped samples, it was assumed that antimony would occupy the tin atom sites. To refine the whole pattern, Thompson-Cox-Hastings pseudo-Voigt axial divergence asymmetry (TCH) profile function was used. As asymmetry is dominant at lower angles, asymmetry was considered for refinement of the peaks at 2θ below 30°. Refinement was performed using Young guidelines and refined till a chi^2 value of nearly 2 was reached. The square root of the chi^2 value gave the goodness of fit (GOF) for the profile. The plots after refinement are all depicted in Figure 3. The observed, refined and difference patterns are shown in Figure 3(a). Phase purity of the material can be seen as no secondary phases were observed. The refined structural

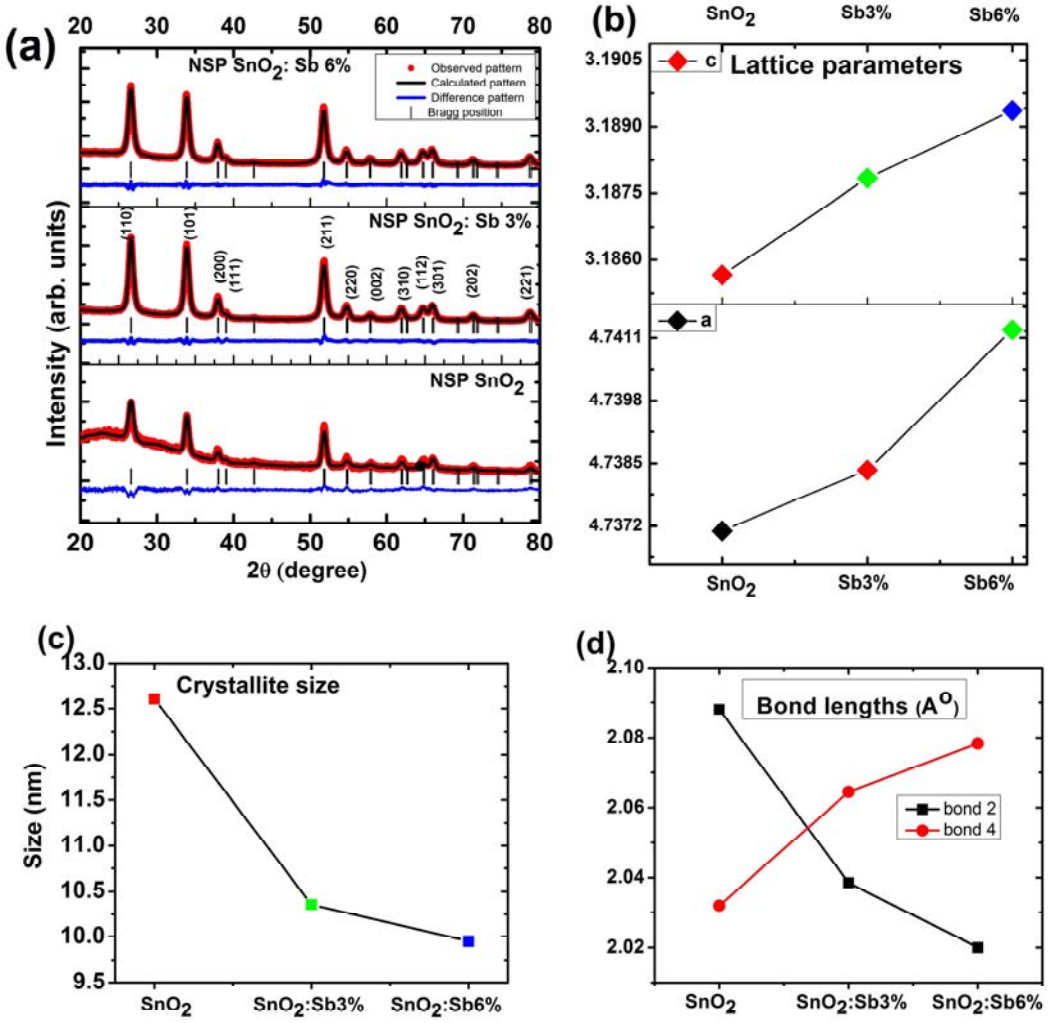

Figure 3 (a) FULLPROF plots after refinement (b) Variation of lattice parameters (c) Crystallite size (d) Bond lengths

parameters are given in Table 1. It is clear that as doping concentration increased the lattice parameters a and c increased while the c/a ratio remained constant. The increase in lattice parameters resulted in an increase in the volume of the unit cell with increasing concentration of antimony. The increase in lattice parameter with increased concentration of Sb is shown in Figure 3(b).

To calculate the accurate sizes of the crystallites, anisotropy in the particles was considered and average crystallite size of the particles was calculated by employing a Lorentzian anisotropic size broadening (spherical harmonics) model. During refinement, instrument standard values were not refined. The acquired values of the average crystallite sizes with respect to the doping content are plotted in Figure 3(c), and it is clear that the average crystallite size decreased from 12.5 nm in the case of the undoped SnO_2 to 10 nm for the 6% antimony-doped SnO_2. The decrease in size with increased antimony content was due to the dopant creating a layer on the surface of the particles which inhibited the growth of the crystallites.

In cassiterite SnO_2, the tin atom is surrounded by six oxygen atoms and forms an octahedron. Among the six Sn-O bonds present, two have one bond length while the remaining four bonds have another bond length. The FULLPROF® Rietveld refinement suite is equipped with a program 'Bond_Str', which enabled the calculation of the bond lengths by taking input from the crystallographic information file generated after pattern refinement. The calculated bond lengths and its variation with dopant concentration are presented in Figure 3(d).

3.2. Electron microscopy analysis

Transmission electron microscopy was used to get an idea of the crystallinity of the as-synthesized particles as well as to know the particle morphology and sizes. Transmission electron micrographs for pure SnO_2 and 9% Sb-doped SnO_2 are shown in Figure 4. TEM micrographs show that the particles were mostly spherical in shape with some having a rod-shaped structure. The growth of particles into rod-shaped structures was attributed to the

Table 1Rietveld refinement values

Sample	Sb doping concentration (atom%)	R_p	R_{wp}	Chi^2	*GOF*	*a*(Å)	*c*(Å)	*c/a ratio*	*Density* g/cm^3	*Volume* $Å^3$
SnO_2	0	3.99	5.20	2.59	1.6	4.7371	3.1857	0.6730	7.419	71.486
Sb3	3	3.82	4.80	1.90	1.4	4.7384	3.1878	0.6723	6.714	71.573
Sb6	6	3.80	4.80	1.96	1.4	4.7413	3.1894	0.6723	6.956	71.696

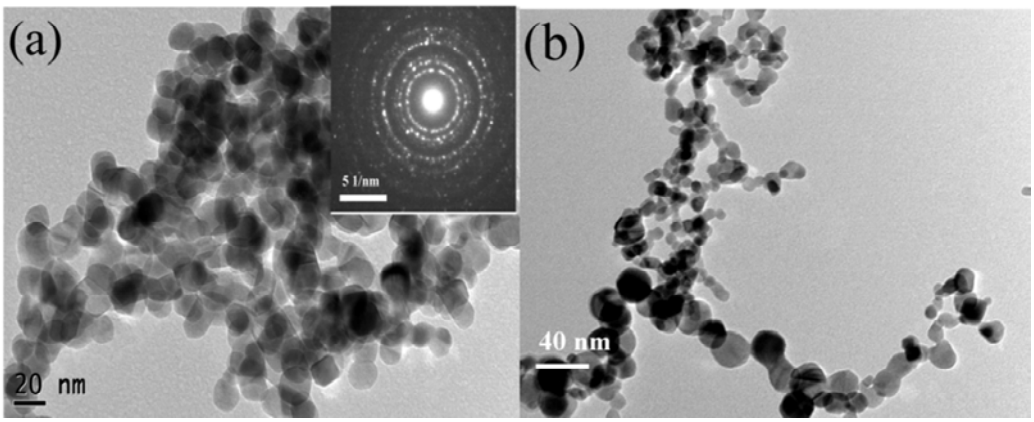

Figure 4 TEM micrographs of (a) SnO_2 (b) SnO_2:Sb6%

tetragonal structure of SnO_2. During Rietveld refinement, use of a preferred orientation along the (110) axis resulted in a value (preferred orientation coefficient G1) nearly equal to 1, which confirmed the presence of a preferred orientation along (110) direction in the sample. In any case, the particles were fairly uniform in the size range of 5 nm – 15 nm. The selected area electron diffraction pattern, given as an inset in Figure 4(a), shows that the particles were crystalline in nature and the diffuse ring pattern confirmed the presence of ultrafine nanocrystals.

3.3. XPS analysis

Doping of antimony in SnO_2 does not result in any extra peaks in the XRD pattern as Sb went into solid solution. To confirm the presence of Sb in doped SnO_2, XPS spectra were recorded for 6% Sb and 9% Sb-doped SnO_2 samples and these are presented in Figure 5. An initial surface scan of the samples, shown in Figure 5(a) and (d) show the presence of tin and antimony doublets with high intensity. The presence of carbon was also evident and arose from the carbon tape. Selective scans for Sn and Sb were performed for both the samples which are also shown in Figure 5. Figure 5(b) and (e) show the Sn doublets at 487.5 eV and 495.8 eV from $3d_{5/2}$ and $3d_{3/2}$ respectively for the 6% Sb-doped samples, and 487.6 eV and 496.0 eV from $3d_{5/2}$ and $3d_{3/2}$ for the 9% Sb-doped samples. Figure 5(c) and (f) show the Sb doublets at 531.5 eV and 540.8 eV from $3d_{5/2}$ and $3d_{3/2}$ respectively in case of the 6% Sb doped samples and 531.7 eV and 541.1 eV from $3d_{5/2}$ and $3d_{3/2}$ respectively for the 9% Sb doped samples. The intense peak of O 1s overlapped with the Sb oxide ($3d_{5/2}$) peak. Energy position of the oxide peak indicated that it had contributions from Sb_2O_3, and Sb_2O_5. The peak of Sb $3d_{3/2}$ transition was centered at 540 eV in the sample and binding energy corresponded to Sb^{5+}. Thus, no Sb^{3+} was detected on the surface.

3.4. Absorption spectroscopy and optical properties

The absorption spectra for the undoped and Sb-doped SnO_2 samples gave an idea of the transparency of the as-synthesized powders in the 100 nm to 1000 nm wavelength region. The spectra are shown in Figure 6(a) and it is obvious that both SnO_2 and Sb-doped SnO_2 particles were transparent to the visible spectrum (400 nm to 600 nm range). For all the powders synthesized, the transparency was greater than 80% in the visible regime. In all the cases, the absorption increased significantly when the excitation wavelength decreased to less than about 300 nm. From the absorption spectra, Tauc plots were generated for the estimation of the direct band-gap energy. The

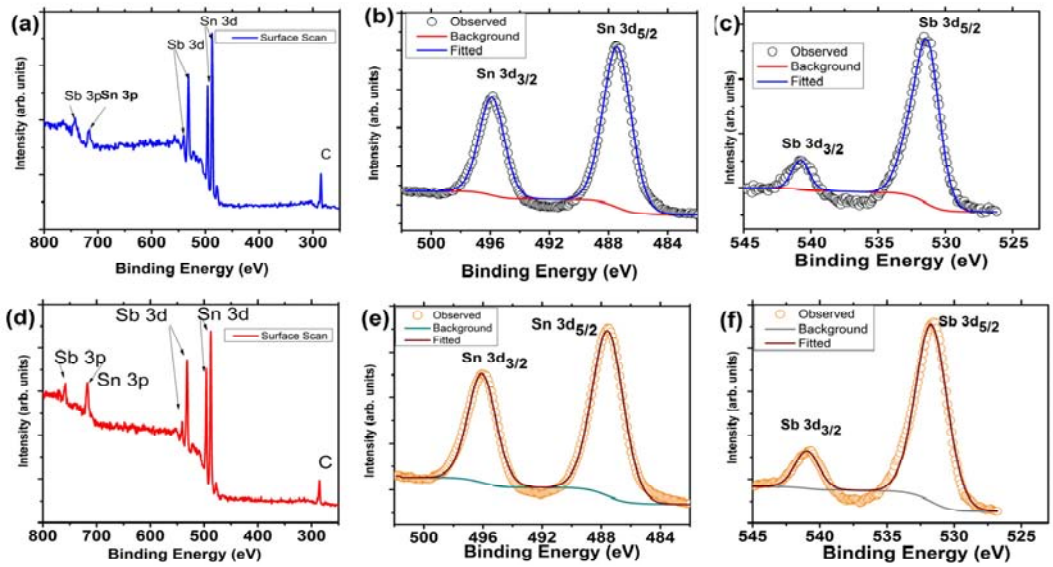

Figure 5 XPS plotsof (a)-(c) SnO_2:Sb6%; (d)-(f) SnO_2:Sb9%

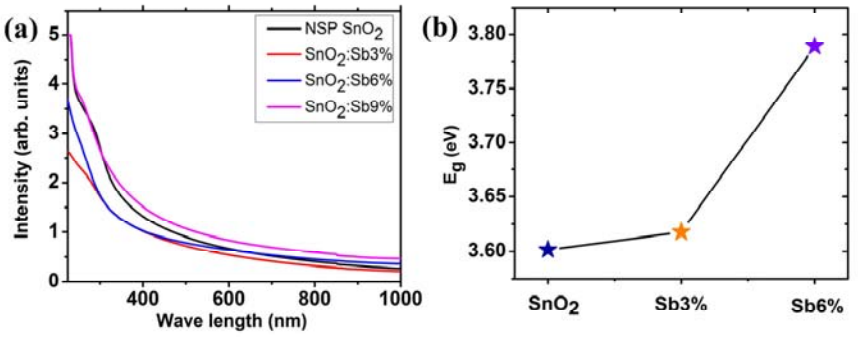

Figure 6 (a) Absorption spectra (b) Energy bandgaps

variation of the bandgap energy with the Sb doping content is presented in Figure 6(b). The increase in the band-gap energy with increasing Sb content was attributed to the presence of Sb as well as the decreasing crystallite sizes.

4. Concluding Remarks

Using a nebulized spray pyrolysis route pure SnO_2 and antimony-doped SnO_2 particles in the ultrafine, nanocrystalline form were synthesized using inorganic precursors. The as-synthesized powders were phase pure SnO_2 and no impurities or secondary phases could be detected. By Rietveld refinement using spherical harmonics, the lattice parameters and crystallite sizes were computed. With increasing Sb content the lattice parameters increased (because of the larger Sb atom) while the crystallite sizes decreased (growth inhibition due to Sb presence). Transmission electron microscopy confirmed that the particles were highly nanocrystalline with sizes ranging from 5 nm to 15 nm in all the cases. X-ray photoelectron spectroscopy confirmed the presence of antimony in the doped samples. The as-synthesized powders were transparent in the visible range and the band-gap energy was 3.6 eV in the case of pure nanocrystalline SnO_2 which increased to 3.8 eV on doping with 9% Sb.

5. References

[1] T. Minami, Semicond. Sci. Technol. 20 (2005) S35–S44
[2] E. Fortunato, D. Ginley, H. Hosono, D.C. Paine, MRS Bull. 32 (2007) 242–247
[3] Z.M. Jarzebski, J.P. Marton, J. Elctrochemical Soc. (1976) 199–205
[4] T. Nutz, M. Haase, J. Phys. Chem. 104 (2000) 8430–8437
[5] M.-M. Bagheri-Mohagheghi, N. Shahtahmasebi, M.R. Alinejad, A. Youssefi, M. Shokooh-Saremi, Phys. B Condens. Matter. 403 (2008) 2431–2437
[6] D.S. Ginley, Handbook of transparent conductors, Springer, 2010
[7] J. Montero, C. Guillén, J. Herrero, Surf. Coatings Technol. 211 (2012) 37–40
[8] V. Senthilkumar, P. Vickraman, M. Jayachandran, C. Sanjeeviraja, J. Mater. Sci. Mater. Electron. 21 (2010) 343–348
[9] B. Orel, J. Mater. Sci. 27 (1992) 313–318.
[10] T. Nütz, U. Zum Felde, M. Haase, J. Chem. Phys. 110 (1999) 12142–12150
[11] L.R.B. Santos, T. Chartier, C. Pagnoux, J.F. Baumard, C. V Santillii, S.H. Pulcinelli, A. Larbot, J. Eur. Ceram. Soc. 24 (2004) 3713–3721
[12] J. Zhang, L.G. Ã, J. Solid State Chem. 177 (2004) 1425–1430
[13] L. Kőrösi, S. Papp, S. Beke, B. Pécz, R. Horváth, P. Petrik, E. Agócs, I. Dékány, Appl. Phys. A. (2012) 1–8
[14] J. Kling, H. Hahn, J. Nanoparticle Res. 12 (2010) 2579–2588
[15] B.M. Jolly, S.K. Ravi, S. Ipe, S.S. Bhattacharya, Trans. Indian Inst. Met. 68 (2015) 147–151
[16] M.J.S. Raju, G.R. Reddy, S. Basu, S.S. Bhattacharya, Nanotechnol. ,IEEE 15th Int. Conf. (2015) 385–388